Proceedings World Geothermal Congress 2023
Beijing, China, October 9 – 11, 2023

# Borehole seismic study at the Utah FORGE geothermal site, USA

Y. Li[1, 3], D. Li[2], L. Huang[2], Y. Zheng[3], and J. Moore[4]

[1]BlueSkyDas LLC, TX 77479, USA; [2]Los Alamos National Laboratory, NM 87545, USA; [3]University of Houston, TX 77004, USA; [4] University of Utah, UT 84108, USA

y1p2li58@gmail.com; davidzli@lanl.gov; ljh@lanl.gov; yzheng24@central.uh.edu; jmoore@egi.utah.edu

**Keywords:** Enhanced Geothermal Systems (EGS), Borehole Seismic, 3-Component (3C) Geophones, Distributed Acoustic Sensing (DAS), Fracture Stimulations, Induced Micro-seismicity, Shear-Wave Splitting, Anisotropic Media

## ABSTRACT

Geothermal energy is a clean, renewable resource. Characterizing geologic formations near geothermal wells is crucial for safely extracting heat energy from underground. Seismic observation systems play important roles in monitoring various effective fracture stimulations to extract geothermal energy from reservoirs of enhanced geothermal systems (EGS). In this study, we use microseismic waveforms acquired during Phase 2C of the Utah FORGE (Frontier Observatory for Research in Geothermal Energy) project in 2019 and a catalog of induced micro-earthquakes during the Phase 2C stimulations available at the U.S. Department of Energy (DOE) Geothermal Data Repository (GDR). We examine and compare waveforms of micro-earthquakes recorded using both a distributed acoustic sensing (DAS) system and a geophone array with twelve 3C sensors deployed in the observation well (78-32) when three stages of fracture stimulations were carried out in the treatment well (58-32). We use an induced micro-earthquake catalog to characterize seismicity associated with the Phase 2C stimulations and derive b-values of 424 induced micro-earthquakes in Stages 1, 2, and 3 of fracture stimulations. We find that the b-values vary with time. We employ eigenvector rotation and waveform correlation to separate fast and slow S-waves, determine their directions, measure the lag time between $S_1$-wave and $S_2$-wave, and calculate S-wave Splitting Rate (SSR) for 6 and 3 induced micro-earthquakes in Stages 1 and 3 of fracture stimulations, respectively. We find the SSR values increase with time between Stages 1 and 3 of fracture stimulations. The time-lapse increases of both SSR values and b-values may be related to heavily fractured zones created by 317 micro-earthquakes during the Stage 2 fracture stimulations. Highly variable and large SSR values in Stage 3 may reflect heterogeneities of the fracture zones created by the Stage 2 stimulations. Time-lapse variations of SSR values and b-values may be useful for monitoring and characterizing the effectiveness and efficiency of various fracture stimulations.

## 1. INTRODUCTION

Enhanced Geothermal Systems (EGS) provide alternative clean energy. The Utah FORGE EGS site is located in Beaver County, Utah, USA, which is a field laboratory to test various stimulation methods and characterize physical properties of different subsurface formations in the EGS reservoirs and surrounding areas. Better understanding of anisotropic and other physical properties of EGS reservoirs and surrounding media is crucial for monitoring and evaluating effective fracture stimulations. Downhole observation systems are essential for monitoring micro-earthquakes induced by fracture stimulation cycles. Distributed Acoustic Sensing (DAS) systems and three-component (3C) geophone arrays were deployed in several shallow observation wells to acquire microseismic waveforms during fracture stimulations in the deep treatment wells. We analyze microseismic waveforms acquired in Phase 2C fracture stimulations and use a catalog of induced micro-earthquakes in our study. We examine and compare waveforms recorded using both a DAS system and a 3C geophone array. We characterize induced seismicity and derive b-values of micro-earthquakes in Stages 1, 2, and 3. We observe time-lapse increases of b-values. We employ the eigenvector rotation and waveform correlation methods for analyzing Shear-wave (S-wave) splitting. Then, we calculate and compare S-wave Splitting Rate (SSR) values for 6 and 3 induced micro-earthquakes in Stages 1 and 3 of fracture stimulations, respectively, and find time-lapse increases of the SSR values. Finally, we present time-lapse increases of both SSR values and b-values and discuss implications of these important findings.

## 2. UTAH FORGE SITE, DOWNHOLE OBSERVATION SYSTEMS AND SEISMIC WAVEFORMS

### 2.1 Utah FORGE site and geothermal wells

FORGE stands for the Frontier Observatory for Research in Geothermal Energy. The Utah FORGE site is one of field underground laboratories used to test and develop Enhanced Geothermal Systems (EGS) technologies (Moore et al, 2020). Geological map in Figure 1a shows a geographic location of the Utah FORGE geothermal site in Beaver County, Utah, USA, with geological features and several vertical and deviated wells drilled in the geothermal test facility for a series of experiments. The treatment well (58-32) is a near-vertical well that was drilled to a depth of about 2297 m with high temperature of 200°C for characterizing an EGS fracture stimulation zone in the granitic basement host rock. A series of fracture stimulations have been carried out in this well. A vertical monitor well (78-32) was drilled to a depth of 1000 m (Fig. 1b), with a maximum temperature of 134°C. The seismic observation systems deployed in the observation well 78-32 were used to monitor induced micro-earthquakes during the fracture stimulation cycles in the treatment well 58-32.

### 2.2 Downhole seismic observation systems

Downhole seismic observation systems at the Utah FORGE site used for this study include a DAS interrogator unit with a 1-km long fiber-optic cable cemented outside of the well casing and 12 three-component (3C) geophones deployed in the monitor well 78-32 (Figs 2a & 2b). The geophone array sensors were deployed at depths from 645 m to 980 m, with a sensor depth interval of 30.48 m and a time sampling rate of 0.5 ms. The DAS system with a channel spacing of 1 m, gauge length of 10 m, and time sampling rate of 0.5 ms continuously recorded microseismic data. During Phase 2C of the Utah FORGE project between April 19 and May 3, 2019, the borehole geophone array recorded 424 locatable induced micro-earthquakes (Figs. 2a & 2b) with magnitudes ranging from -0.52 to -2.0 during stimulation cycles (Stages 1, 2, and 3) in treatment well 58-32 (Pankow et al., 2020).

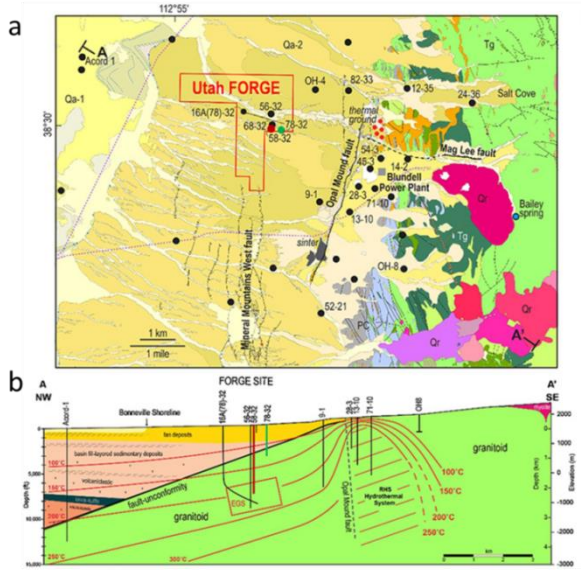


**Figure 1: a. Geological map shows the Utah FORGE location with a deviated and several vertical geothermal wells drilled at this EGS site. b. The treatment well 58–32 (red) was drilled through fan and sediment deposits and reached the geothermal reservoir (EGS) in the low permeability granite rocks at a depth of 2294 m with a temperature of about 200°C. The observation well 78–32 (green) was drilled to a depth of 1000 m with a maximum temperature of 134°C at the bottom of the well (modified from Li et al, 2022).**

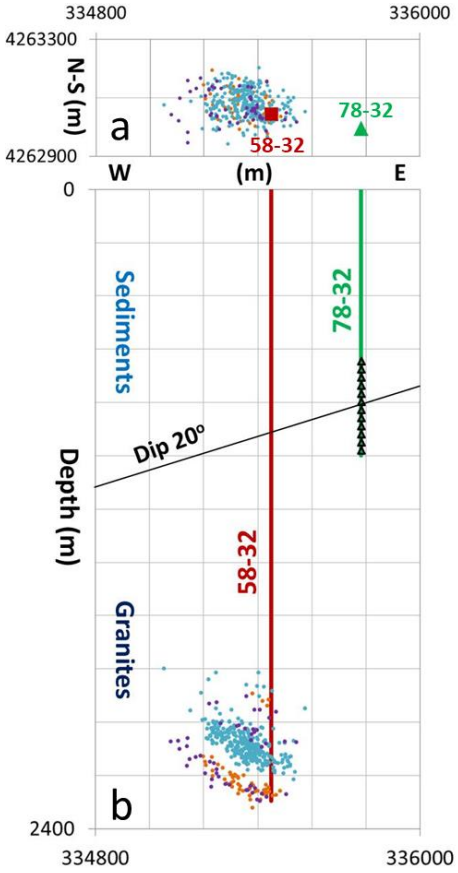


**Figure 2: Map view (a) and cross-section (b) show a treatment well (58-32) and a monitor well (78-32) with a DAS system and twelve 3C geophones installed in the well, and micro-earthquakes induced by different fracture stimulation cycles (with different color codes) in the treatment well. There is a dipping interface between fan and sediment deposits and granitic rocks.**

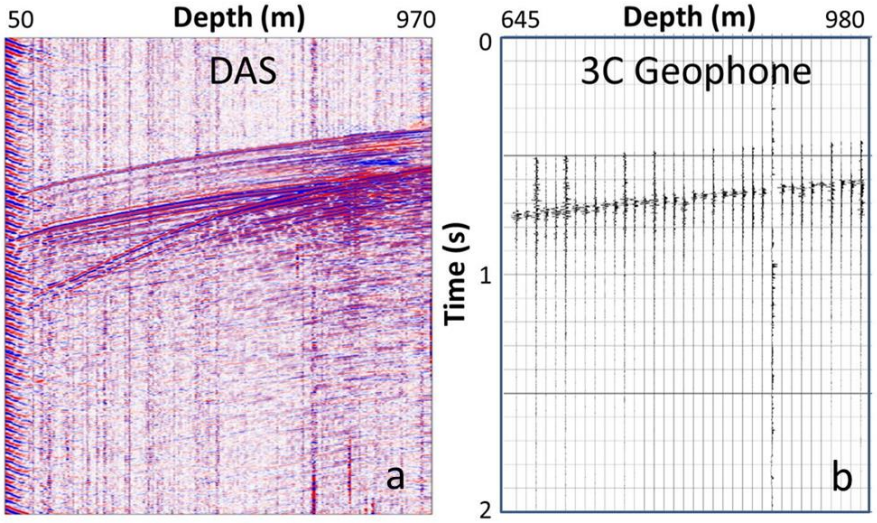


**Figure 3: An induced micro-earthquake with a magnitude of -0.52 recorded using (a) a DAS system with about 1 km fiber cable with "sensor" spacing of 1 m and (b) twelve 3C geophones deployed at depths from 645 to 980 m, with a geophone spacing of 30.48 m. Both P and S waves are recorded using the DAS and geophone monitoring systems.**

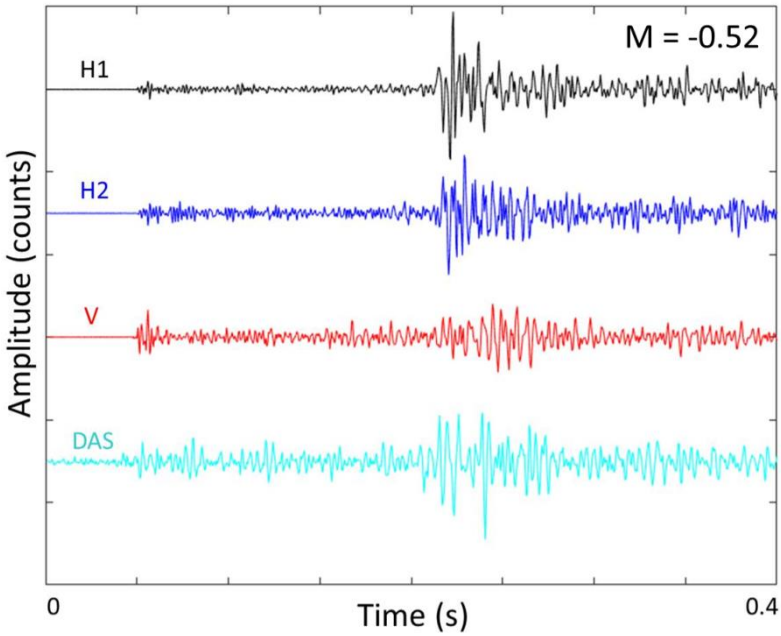


**Figure 4: Comparison of seismograms of an induced micro-earthquake (M=-0.52) recorded using a 3C geophone and the DAS fiber sensor at a depth of 950 m.**

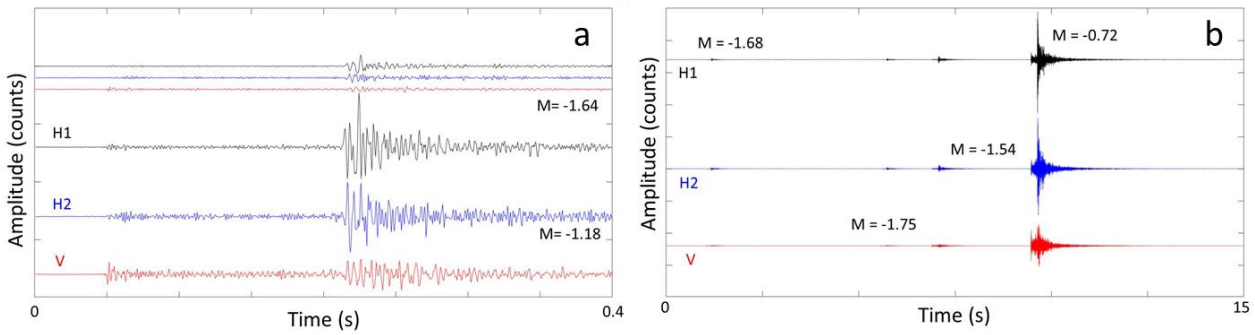


**Figure 5: a. 3C seismograms of two nearby micro-earthquakes with different magnitudes display high similarity of waveforms. b. 3C seismograms of four seismic events occurred within less than 10 seconds with one magnitude difference show high similarities of waveforms.**

### 2.3 Downhole seismic waveforms from DAS and geophones

During Phase 2C of the Utah FORGE project, downhole DAS and 3C geophone systems in the monitor well 78-32 recorded T-bytes microseismic waveform data during three stages of fracture stimulations in the treatment well 58-32. These microseismic waveform data sets enable a comprehensive seismic study of induced micro-earthquake locations, relationship between seismic activities and the injection process, micro-earthquake source characterization and rupture process, and rock anisotropic properties in the EGS zone and surrounding regions.

Figures 3a and 3b show seismograms recorded using a DAS system of about 900 usable channels and a geophone array of twelve 3C sensors, both with a time sampling rate of 0.5 ms. The DAS channel spacing is 1 m and the geophone depth interval is 30.48 m. P-wave, S-wave, and converted SP-wave are clearly observable on the DAS seismogram (Fig. 3a). The very fine spatial resolution of 1 m for the DAS recordings ensures continuation of those seismic signals. However, DAS data are relatively noisy, with a low signal-to-noise ratio (SNR), and single-component data with an effect of fiber directivities. Disadvantages of 3C geophone seismograms (Fig. 3b) include a sparse sensor spacing of 30.48 m and a small depth range of coverage from 645 to 950 m compared with that of the DAS recordings. The most important feature of 3C seismic recordings is that we can measure which direction of seismic energy coming from if the 3C geophones are accurately and reliably calibrated. This feature of the 3C geophone makes it an appealing tool for analyzing shear-wave splitting and relative seismic event locations with high accuracy.

We compare seismograms (Fig. 4) of an induced micro-earthquake (M= -0.52) recorded with a 3C geophone and a DAS channel at the same depth of 950 m. The 3C geophone with one vertical and two horizontal components records particle velocity or acceleration depending on instruments used, while the DAS system measures the strain rate at the position. Therefore, it is expected to have some phase differences between the DAS seismic trace and geophone seismic traces. The DAS trace is noisier than those geophone traces when comparing noise levels prior to the P-wave first arrivals. We recommend making an Eigen-vector rotation of 3C geophone data to the ray direction and two orthogonal directions, and then comparing with P-wave and S-wave waveforms on the DAS recording after directivity corrections.

Figure 5a displays 3C seismograms of two nearby induced micro-earthquakes with magnitudes of -1.64 and -1.18, respectively. We observe that the arrival times of P- and S-waves are almost the same and there is a high degree of similarities of 3C waveforms. Time-domain and frequency-domain cross-correlation can result in highly accurate arrival-time picks for both P- and S-waves, which would lead to highly accurate relative event locations. This cross-correlation is a very important step toward higher resolution event locations for characterizing the directions, lengths, and heights of fractures and fracture zones. Figure 5b shows 3C seismograms of four consecutive induced micro-earthquakes with magnitudes ranging from -1.75 to -0.72. High similarities of 3C waveforms of those four events suggest the induced micro-earthquakes originated at close positions. Therefore, the waveforms of smaller events can be used as empirical Green's functions and are deconvolved from the waveforms of the larger micro-earthquake, to retrieve the relative source time function of the larger micro-earthquake, resulting in better measurements of the source duration and rising time for reliable estimation of stress drops.

In the following two sections, we focus on characterizing seismicity by analyzing b-values and studying shear-wave splitting to reveal media anisotropy in sedimentary and granitic rocks at the Utah FORGE site.

## 3. SEISMICITY AT UTAH FORGE AND B-VALUE ANALYSIS

### 3.1 Characterization of induced seismicity at Utah FORGE during Phase 2C project

During the Phase 2C project, between April 19 and May 3, 2019, a DAS system and twelve 3C geophones deployed in the monitor well 78-32 recorded a lot of induced microseismic events during three stages of fracture stimulations in the treatment well 58-32. Seismic waveforms of the induced micro-earthquakes recorded using the twelve 3C geophones in the monitor well (78-32) have been analyzed by many researchers. The induced micro-earthquake location results from one of the service providers are available at the DOE Geothermal Data Repository (GDR). We use this catalog of micro-earthquake locations for our characterization of induced seismicity at the Utah FORGE geothermal site.

Figure 6 demonstrates temporal variations of seismic activities during Stages 1, 2, and 3 of fracture stimulation cycles in about 10 days. There are about 424 locatable induced micro-earthquakes during this period of time. The magnitudes of those micro-earthquakes range from -2.0 to -0.52. Numbers of locatable induced micro-earthquakes in Stages 1, 2, and 3 of fracture stimulations are 57, 317, and 50, respectively. Micro-earthquakes induced in Stages 1, 2, and 3 are color-coded with orange, cyan, and purple, respectively. There is an apparent lack of large induced micro-earthquakes with magnitudes larger than -1.0 during Stage 3 of fracture stimulations. Our statistics of percentages of large (M =-0.5 to -0.99), middle (M=-1.0 to -1.49) and small (M=-1.5 to -2.0) micro-earthquakes during the entire fracture stimulation process are 4.7%, 25.3%, and 70%, respectively.

Figure 7 shows the map view (a) and a cross-section (b) of the spatial and strength distributions of 424 induced micro-earthquakes during the entire fracture stimulations. The figure depicts induced micro-earthquakes with a magnitude interval of 0.25 using different symbols. For larger micro-earthquakes with a magnitude larger than -0.99, we plot the events with color-codes orange, cyan, and purple to indicate that they occurred in Stages 1, 2, and 3 of fracture stimulations. We find that the large micro-earthquakes in Stage 2 with a magnitude of larger than -0.99 concentrate in a small region near the treatment well 58-32 in both the map view and the cross-section (Figs 7a and 7b). The map distribution (Fig 7a) of larger micro-earthquakes (M. -0.99) in Stage 1 is relatively scattering, but the micro-earthquake depth distribution (Fig 7b) indicates a fracture zone associated with the larger magnitude micro-earthquakes in Stage 1. There is only one larger micro-earthquake with a magnitude of -0.89 recorded during Stage 3 stimulations.

The interesting spatial distribution patterns of the larger induced micro-earthquakes may be directly related to different stimulation methods. However, the current location results need to be refined using the waveform correlation and relative event location methods to confirm such interesting distribution patterns of induced micro-earthquakes. If the concentrated event distribution pattern of

induced micro-earthquakes in Stage 2 of stimulation is proved to be true, it could have important implications for different types of fracture stimulations.

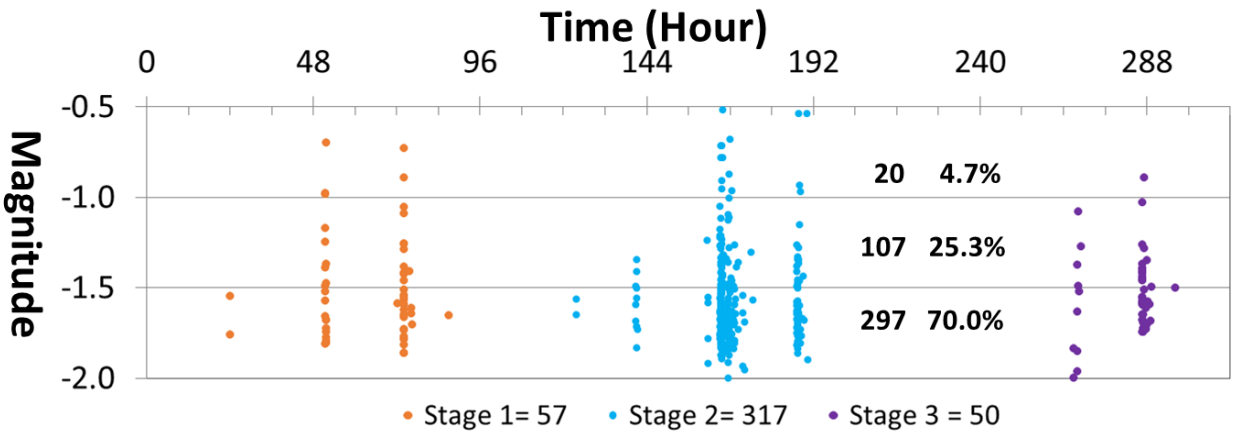


**Figure 6: Temporal variations of induced micro-earthquakes in three stages of fracture stimulations. Microseismic events in different stages are displayed with different colors. It also shows statistics of percentages of large, middle, and small size micro-earthquakes during the entire fracture stimulation process. Time 0 is at 13:58:55 on April 20, 2019 about 24 hours before the first induced micro-earthquake occurred.**

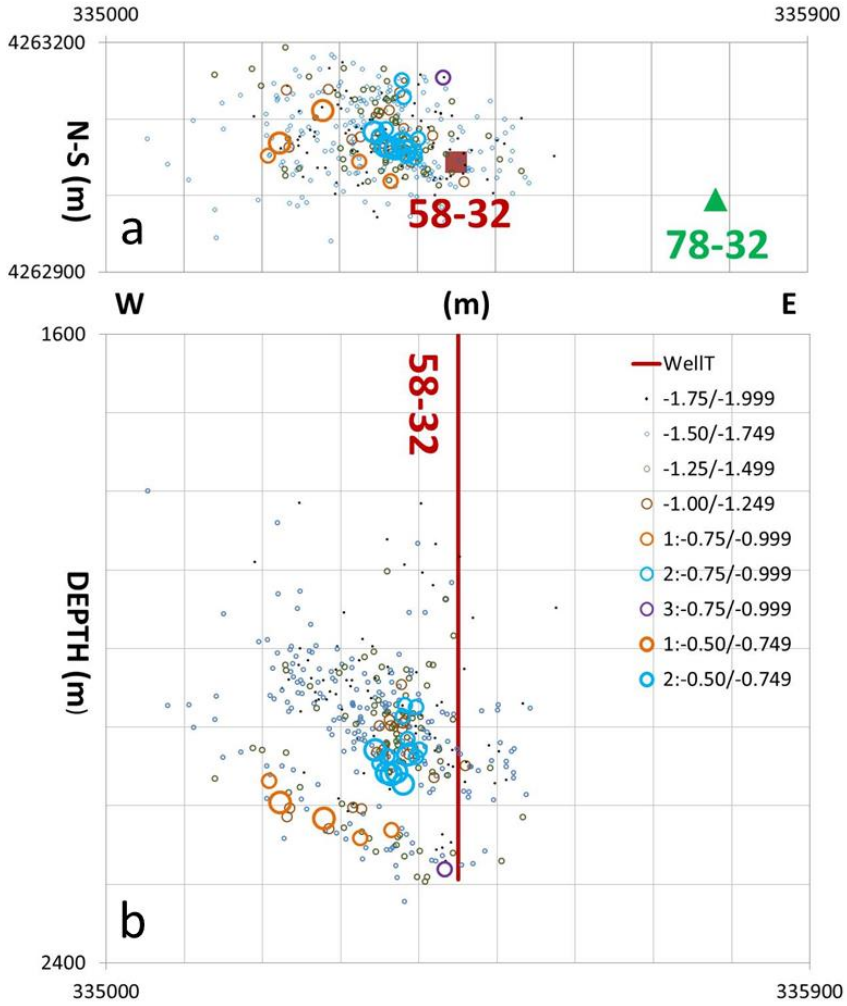


**Figure 7: Spatial and strength distributions of induced micro-earthquakes in a map view (a) and a cross-section (b). Note that larger magnitude (M = -0.999 to -0.5) micro-earthquakes occurred mostly in Stage 2 (color cyan) and rarely in Stage 3 (color purple).**

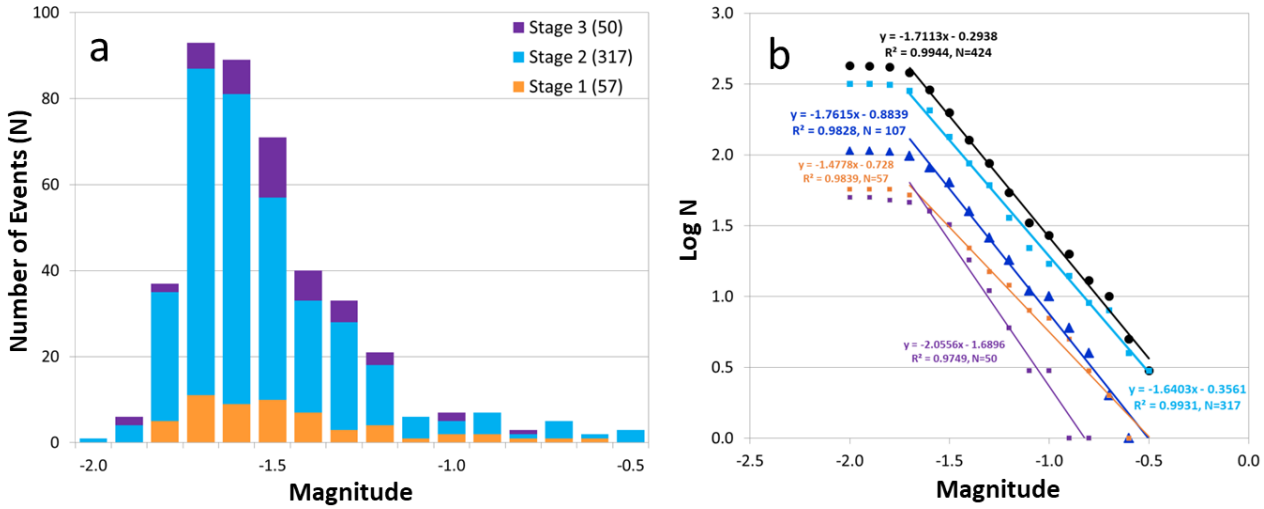


**Figure 8: a. Histogram of induced micro-earthquakes occurred during Stages 1, 2, and 3 of fracture stimulation cycles. b. Estimates of b-values using events in different stages (colors orange, cyan, and purple for Stage 1, 2, and 3 respectively), and 107 events in Stages 1 and 3 (blue triangles and line) among a total of 424 events (solid black circles and line).**

### 3.2 Analysis and comparison of b-values

Figure 8a is a color-coded histogram of induced micro-earthquakes during Stages 1, 2, and 3 of fracture stimulations. During Stage 3 of stimulation, micro-earthquakes with a magnitude larger than -0.99 rarely occurred. Frequency-magnitude distribution of micro-earthquakes can be generally expressed as Log N = a – bM, where N is the cumulative number of micro-earthquakes at a magnitude larger than or equal to M in a given micro-earthquake population, while a and b are constant values, describing the seismicity rate and the proportion of small to large micro-earthquakes, respectively. Geffers et al. (2022) pointed out that the b-value is used not just in earthquake hazard analysis, but also in interpreting material properties, such as heterogeneity, or in inferring the state of stress from given micro-earthquake populations.

The squares in Figure 8b display relationships between the micro-earthquake frequency (Log N) and the magnitude of induced micro-earthquakes in Stages 1, 2, and 3 of fracture stimulations with color codes orange, cyan, and purple, respectively. The black solid circles in Figure 8b depict the relationship for all 424 induced micro-earthquakes during the entire fracture stimulation process. The Log N-M relationship for 107 induced micro-earthquakes during Stages 1 and 3 of stimulations is for reference. The inferred b-values from different micro-earthquake groups are shown in Figure 8b. The b-value derived from all 424 micro-earthquakes is 1.71. The b-values of induced micro-earthquakes in Stages 1, 2, and 3 of stimulations are 1.48, 1.64, and 2.08, respectively, indicating an increase of b-value as a function of time. Since there are only 57 and 50 events during Stages 1 and 3 of stimulations, respectively, the b-values derived from the small numbers of events might not be very accurate.

## 4. SHEAR-WAVE SPLITTING ANALYSIS FOR ANISOTROPIC MEDIA

### 4.1 Analysis method for shear-wave splitting and S-wave splitting rate (SSR)

A shear-wave entering a polar anisotropic medium splits into two S-waves ($S_1$ and $S_2$) with different polarizations propagating with different velocities, with $S_1$ propagating faster than $S_2$. For an anisotropic medium with near-vertical fractures, the $S_1$-wave polarized parallel to the fractures travels faster than the $S_2$-wave polarized perpendicular to the fracture direction. S-wave splitting observed from borehole and surface seismic data is widely used for characterizing the orientation and density of fractures in earthquake seismology and in oil, gas, and geothermal fields (Munson et al., 1993; 1995; Li et al., 1993; Lou and Rial, 1997). Particle motion (hodogram) analysis and eigenvector rotations of 3C seismic data (Li & Hewett, 2016) are two essential steps for characterizing S-wave splitting. We use 3C waveforms of induced micro-earthquakes recorded during the Utah FORGE Phase 2C project to analyze shear-wave splitting for better understanding anisotropic properties of granitic and sedimentary rocks at the Utah FORGE EGS site.

Figure 9a displays 3C raw seismograms of event 1.47 (M=-0.72), with one vertical and two horizontal components of H1 and H2 that are orthogonal to each other, but with arbitrary orientations of geophones at each depth level. We pick the first-arrival time (blue line) of P-wave, Tp, on the vertical component (Fig. 9a). After the eigenvector rotation of two horizontal components, S-waves on H1 and H2 components are rotated to the radial ($S_R$-wave) and tangential ($S_T$-wave) components (Fig. 9b). The arrival times of the S-waves, $T_{SR}$ and $T_{ST}$, can be measured from the radial and tangential components (Fig. 9b), respectively. Figure 9b indicates that $S_R$ is the fast $S_1$-wave and $S_T$ is the slow $S_2$-wave. We derive the origin time of the micro-earthquake using Tp and $Ts_1$ measurements, and calculate travel times of P-wave and $S_1$-wave, tp and $ts_1$, from a source to receivers, respectively. Figure 9 depicts the hodograms (particle motion) (Fig. 9c & 9d) of both P-wave (blue line) and S-waves (red lines) of two horizontal traces (indicated by red arrows in Figs. 9a & 9b) recorded at a depth of 798 m in both H1-H2 (Fig. 9c) and Radial-Tangential (Fig. 9d) coordinate systems. These hodograms also confirm that $S_R$-wave is along the radial direction, the same as that of the P-wave, while $S_T$-wave is perpendicular to $S_R$-wave, on the tangential direction. $S_R$-wave is the fast $S_1$-wave, and $S_T$-wave is the slow $S_2$-wave.

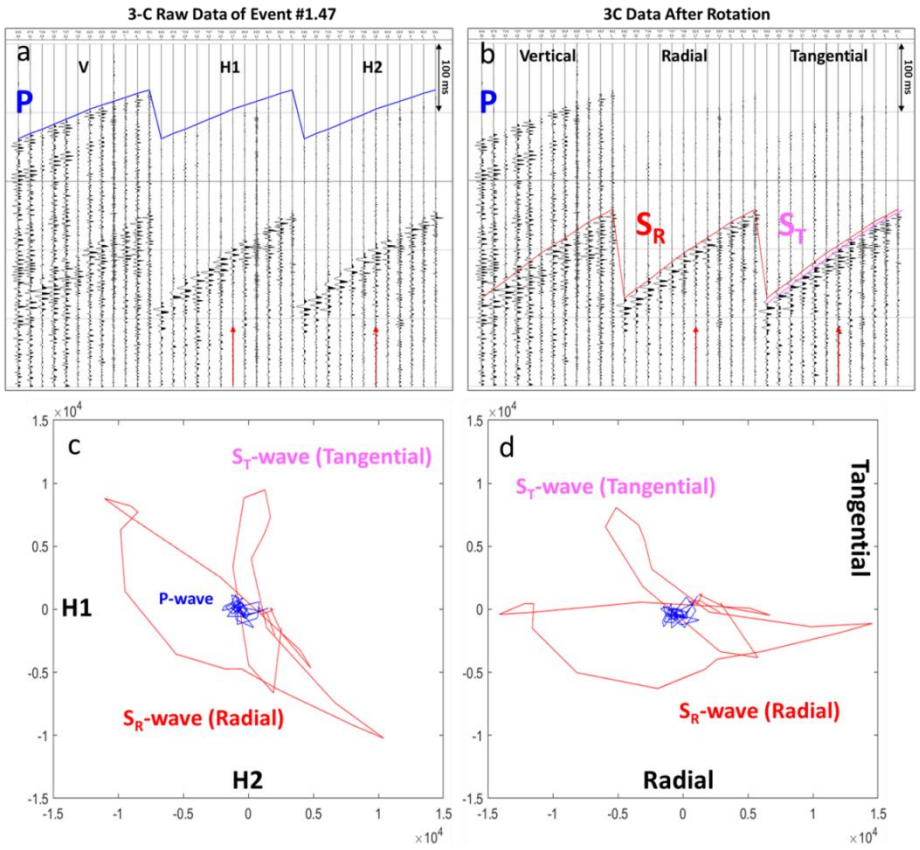


**Figure 9: Three-component seismograms of an induced micro-earthquake (M=-0.72) before (a) and after (b) horizontal component rotations. Picked first arrival times of P-wave, S-waves on the radial ($S_R$) and tangential ($S_T$) components are marked with blue, red, and magenta lines. Hodograms of P-wave and S-waves constructed with two traces indicated by the arrows in (a) and (b) are plotted in the H1-H2 coordinate system before the horizontal rotation (c) and in the radial-tangential coordinate system after the rotation (d). Both rotated seismograms and hodograms indicate that S-waves splitting into $S_R$–wave and $S_T$–wave.**

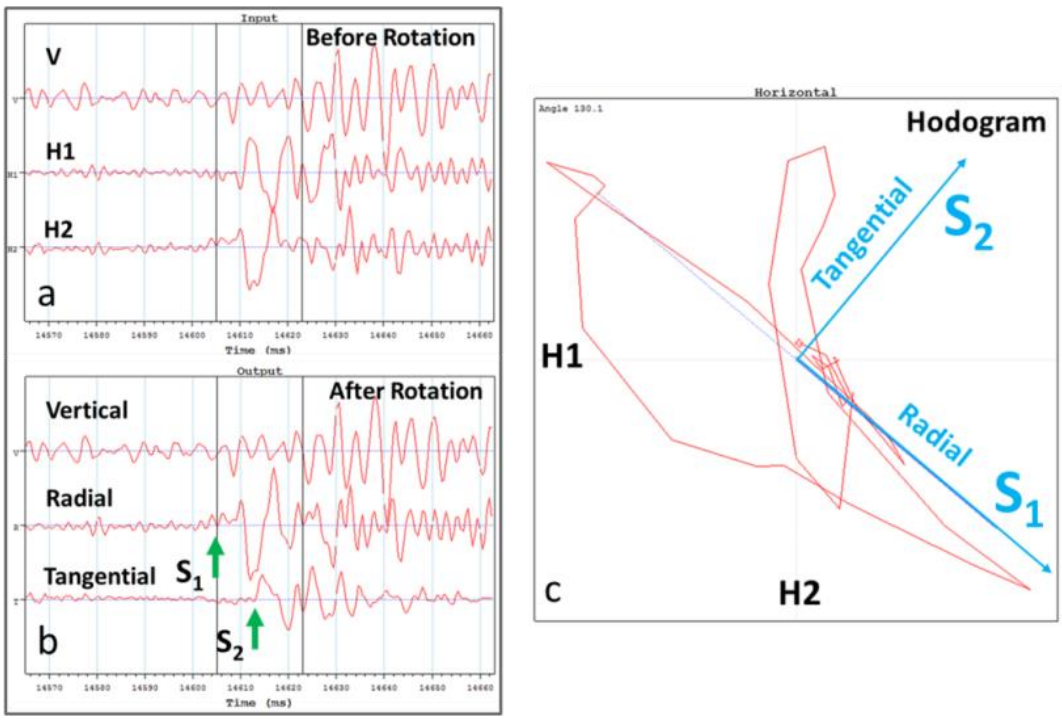


**Figure 10: a. Vertical, $H_1$, and $H_2$ components of raw S-waves before the eigenvector rotation. b. After the horizontal rotation, the fast $S_1$-wave and the slow $S_2$-wave are observed on the radial and tangential components and the amount of shear-wave splitting (lag time) can be quantitatively measured. c. Hodogram demonstrates how $H_1$ and $H_2$ components of S-waves are rotated to the radial and tangential components and shows S-waves are splitting into the fast S-wave ($S_1$) and the slow S-wave ($S_2$) along the radial and tangential directions, respectively.**

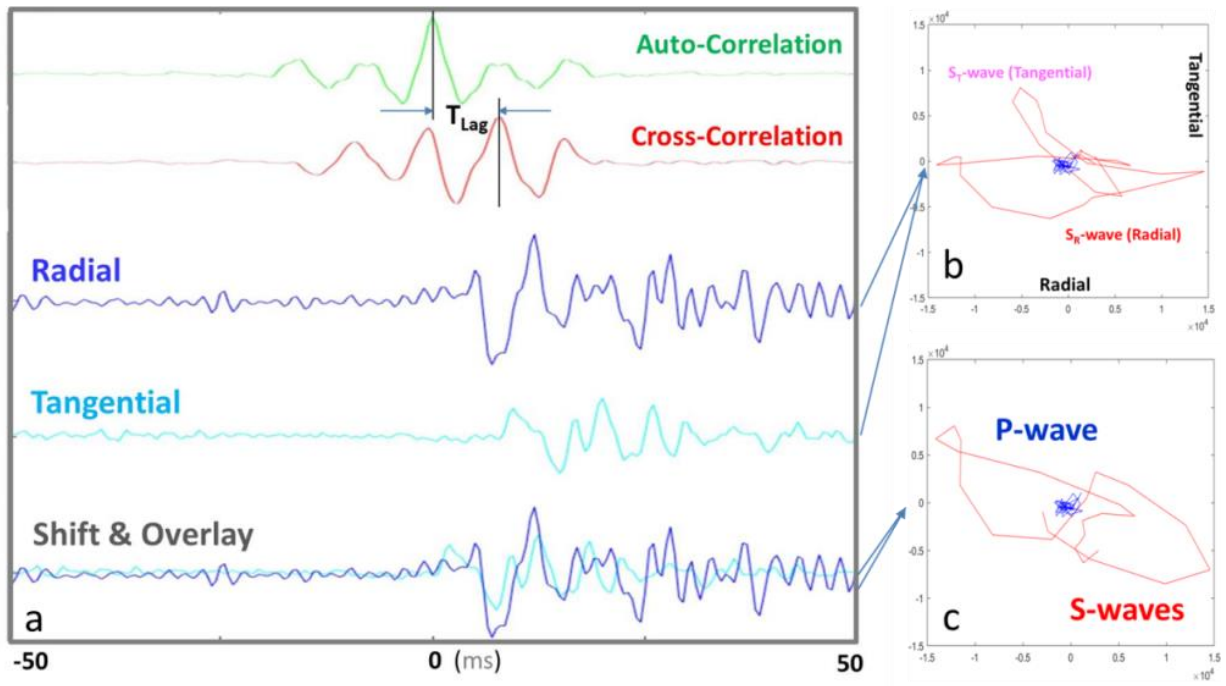


**Figure 11: a. Lag times between the splitting of fast and slow S-waves S1 and S2 can be measured using auto- and cross-correlations of radial and tangential components. b. A hodogram shows S-waves splitting into fast and slow S-waves in the radial and tangential components. c. After shifting the tangential component by an amount of the lag time, a hodogram constructed using two overlaid traces (a) show no S-wave splitting.**

Figures 10 a, b show the time windowed 3-C S-waves of event 1.47 (seismic event #47 in Stage1) recorded by a geophone at a depth of 798 m before and after eigenvector rotation. The $S_1$- and $S_2$-waves are separated (Fig 10b) using an eigen-value calculation and their polarization directions are determined (Fig. 4c). We observe that $S_1$-wave on the radial component is faster than $S_2$-wave on the tangential component (Fig. 4b). The arrival times $T_{S1}$ and $T_{S2}$ can then be picked from the rotated seismic traces on the radial (fast) and tangential (slow) components (Fig. 4c). The S-wave splitting lag time, $dT_{lag}$, is defined as:

$$dT_{lag} = T_{S2} - T_{S1}\,, \tag{1}$$

and the S-wave splitting rate (SSR) can be calculated using

$$SSR = dT_{lag} / t_{s1}\,, \tag{2}$$

where $t_{s1}$ is the travel time of the fast $S_1$-wave from a seismic source to a geophone receiver.

Waveform auto- and cross-correlation can measure time lag $dT_{lag}$ more accurately. The green curve in Figure 11a is the auto-correlation of the radial component, and the red curve is the cross-correlation between the radial and tangential components. We measure time lag $dT_{lag}$ from the two peaks of auto- and cross-correlation curves. Using radial and tangential components, we plot a hodogram to show that S-wave splits into $S_1$-wave and $S_2$-wavein Figure 11b. However, if we shift the tangential component by the amount of time lag and overlay on the radial component (Fig 11a) and use those two traces to construct a hodogram (Fig 11c), no shear-wave splitting is observed.

### 4.2 Shear-wave splitting results for microseismic events in Stages 1 and 3

We analyze shear-wave splitting of six microseismic events occurred in Stage 1 of fracture stimulations recorded using 11 out of 12 geophones in the geophone array at depths ranging from 645 m to 980 m. One geophone at a depth of 889 m was malfunctioned. Figure 12 shows locations of the six events in a map view (Fig.12a) and a cross-section (Fig. 12b), along with positions of treatment and monitor wells. For all six events, we observe that S-waves in the radial directions ($S_1$) are faster than those in the tangential directions ($S_2$). The average azimuth of the fast $S_1$-waves is estimated to be E12.7º±4.5ºS, and orientation of the slow $S_2$-wave is in the direction perpendicular to it (Fig. 12a).

We calculate the S-wave splitting rates (SSR) along ray paths between sources and receivers and display them in Figure 13. The SSR values range from 0.52% to 1.06%. Average SSR values for receivers in granite and sedimentary rocks are 0.72% and 0.91%, respectively. Given the ray paths are mainly in the granite rock, the contribution of the shear-wave splitting in the sedimentary rock is greater than that in the granite rock. For comparison, we show in Figure 13 an anisotropic measurement from sonic dipole logging data acquired in the treatment well 58-32. Because there is a 20° dip (Fig. 2b) in the geological formation (Moore et al, 2020), we subtract 124.5 m from the measured depth of the treatment well 58-32 logging data to account for this dip. The SSR values derived from borehole seismic data are comparable with or larger than those derived from sonic dipole logging data since the sonic logging measures anisotropic near the wellbore only. There is an apparent trend that the SSR values increase with depth in the sedimentary rocks for both sonic and borehole seismic data. By contrast, the SSR values decrease with depths in the granite rocks (Fig. 13). Since

there were not created fractures before Stage 1 stimulation in this zone, SSR results from events in Stage 1 can be used as the base line or reference.

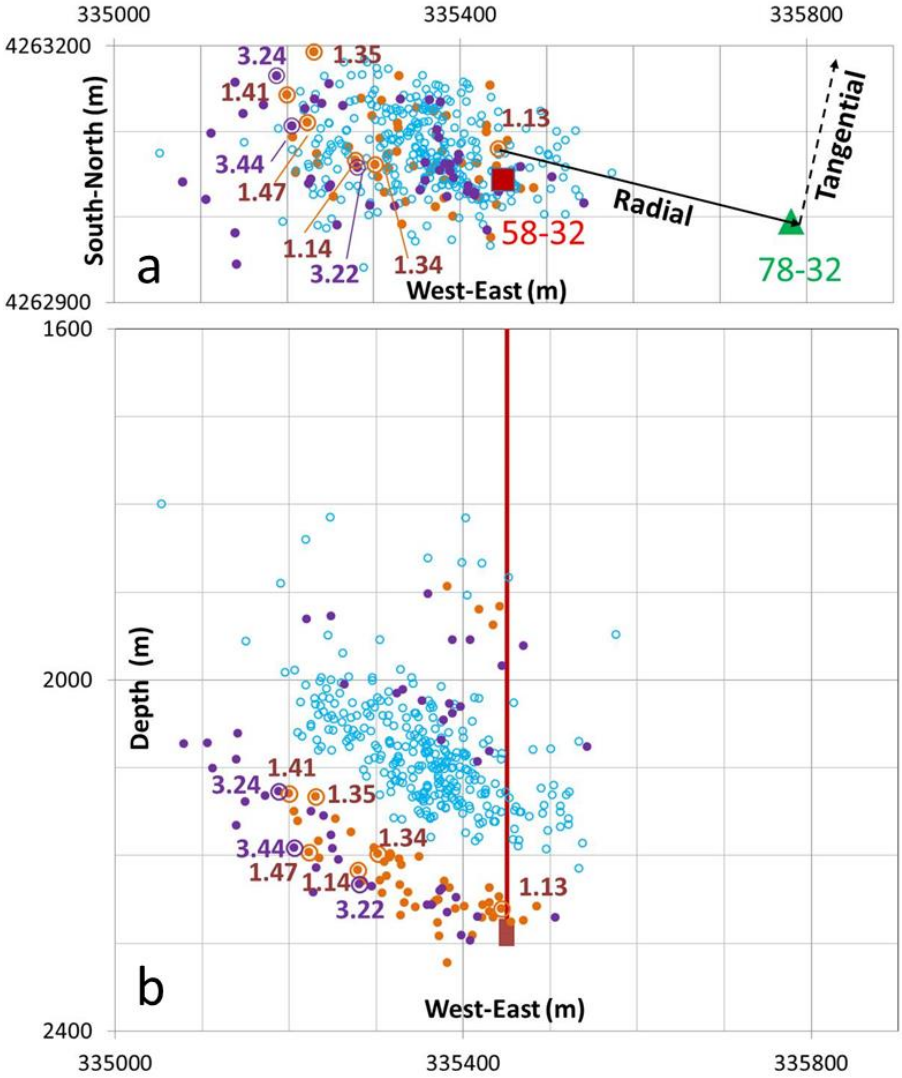


**Figure 12: A map view (a) and a cross-section (b) of microseismic event locations show locations of 6 and 3 microseismic events induced in Stages 1 and 3 of fracture stimulations, along with positions of treatment (58-32) and monitoring (78-32) wells.**

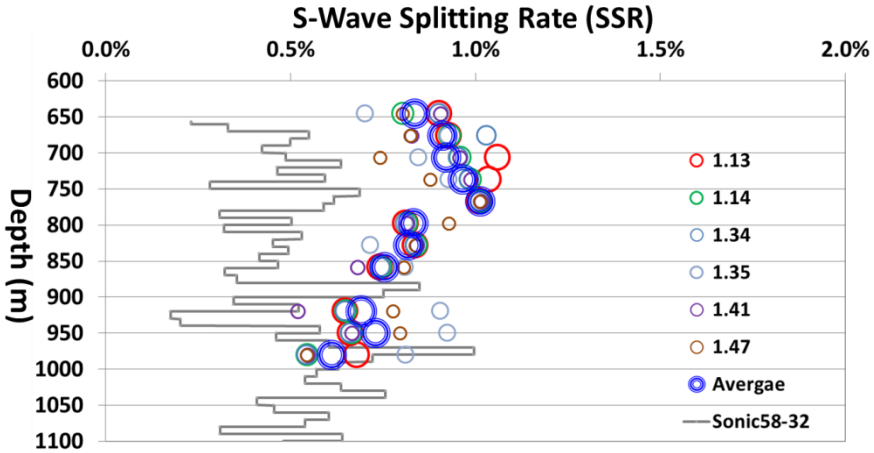


**Figure 13: Shear-wave splitting rates (SSR) of six seismic events in Stage 1 range from 0.52% to 1.06%, and the average SSR values at each depth level are displayed with blue symbols. Dipole sonic logging data (black line) acquired from the treatment well (58-32) is shown for comparison. SSR values in sediments are slightly bigger than those in the granite rocks.**

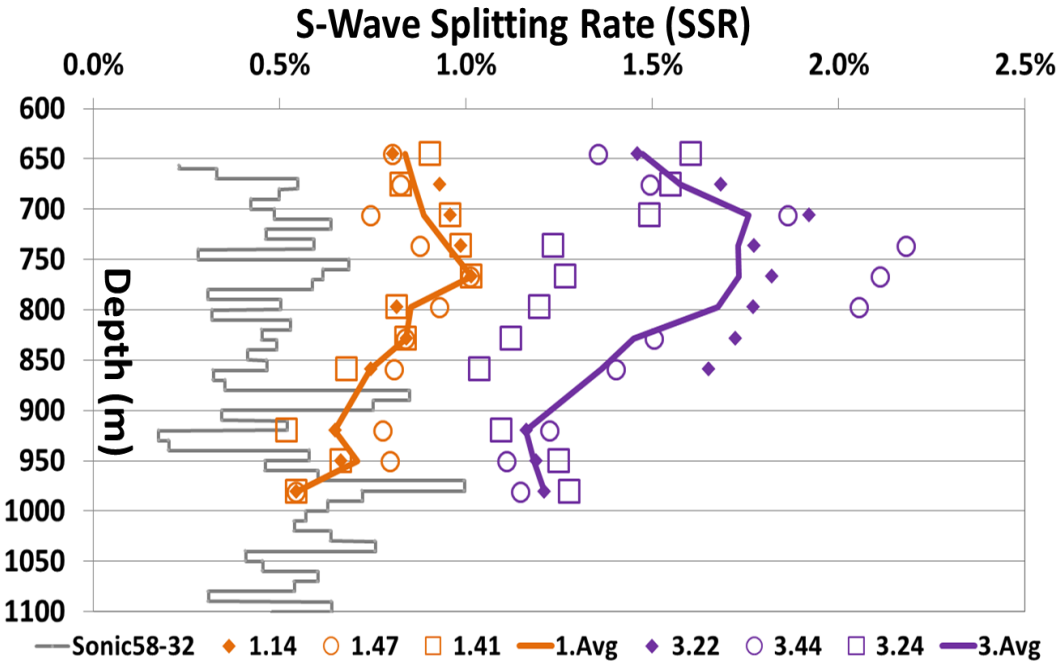


**Figure 14: Comparison of average SSR curves for microseismic events in Stages 1 and 3. Trends of curves are similar to that of sonic dipole log data. Highly variable SSR values of events in Stage 3 suggest high heterogeneities of the fracture zones created by Stage 2 stimulations.**

We analyze S-wave splitting and derive SSR values using 3 micro-earthquakes recorded in Stage 3 (see Fig. 12a, b) of fracture stimulations to search for time-lapse variations of SSR. Figure 14 depicts these SSR values of three pairs of events along with their average value. The average SSR for events in Stage 3 is higher than that for events in Stage 1 (Fig. 14) of fracture stimulation. We hypothesize that higher SSR values for events in Stage 3 may be attributed to the highly fractured media during Stage 2 of fracture stimulations. Significant variations of SSR values for events of Stage 3 may be attributed to heterogeneity of the fracture zones during Stage 2 stimulation.

Figure 12a depicts epicenters of all 424 locatable induced micro-earthquakes. Fast $S_1$-wave is along a radial direction at about E12.7°±4.5°S, which is consistent with the major-semi axis orientation of induced micro-earthquake distribution in Figure 12a. This radial direction is along the dominant fracture directions in the fracture zone and the direction of maximum horizontal stress. $S_1$-wave travelling in this direction is fast, compared with a slow $S_2$-wave that propagates in a direction perpendicular to fracture orientations. A cross-section in Figure 12b shows a depth distribution of all 424 induced micro-earthquakes where 9 events used in this study are marked by large open circles. Between Stage 1 and Stage 3 of stimulations, 317 induced micro-earthquakes occurred during Stage 2 of fracture stimulation, which resulted in highly cracked zones of fractures in the medium between induced micro-earthquake sources in Stage 3 and geophones deployed in monitor well 78-32. This result implies that a large number of induced micro-earthquakes occurred during Stage 2 stimulations may be a possible cause for apparent increase of SSR values derived from induced micro-earthquakes in Stage 3 of stimulations. We hypothesize significant variations of average SSR values derived from Stage 3 events may be related to high heterogeneity in the fracture zones caused by the Stage 2 fracture stimulation. Spatial and strength distributions of induced micro-earthquakes during Stage 2 of fracture stimulation in Figures 7a and 7b confirm that such heterogeneity indeed exist in the fracture zones during Stage 2 stimulation.

### 4.3 Temporal variation of SSR values and b-values

Figure 15 compares trends of temporal variations of SSS values and b-values during the entire fracture stimulation cycles in Phase 2C of the Utah FORGE project from April 19 to 3 May 3, 2019. Figure 15a shows that SSR values in sedimentary rocks are 0.91% in Stage 1 and increase to 1.84% in Stage 3. In granite rocks, SSR values of 0.72% in Stage 1 increase to 1.39% in Stage 3. Figure 15b shows that b-values in Stages 1, 2, and 3 are 1.48, 1.64, and 2.06, respectively, and demonstrates an apparent increase of b-value from Stage 1 to Stage 3. The b-value derived from all 424 induced micro-earthquakes in the entire fracture stimulation process is 1.71 (Figure 15b). This same increase trend may just be a coincidence. However, we cannot rule out the possible correlation between these two parameters, since both are used to characterize heterogeneity of cracked materials, including fractures and fracture zones in rocks.

## 5. CONCLUSIONS

We have analyzed seismic waveforms and location catalog data of 424 micro-earthquakes induced by fracture stimulation cycles in Phase 2C of the Utah FORGE project from April 19 to May 3, 2019. These seismic waveforms were acquired using a DAS system with 1-km long of optic-fiber cable and a geophone array with twelve 3C sensors in the monitor well (78-32) during various fracture stimulation tests in the treatment well (58-32). Endurable features of optic-fibers under high-pressure and temperature in a downhole harsh environment make DAS an appealing tool to acquire seismic data in high-temperature geothermal wells (Li et al, 2021). The DAS systems at the Utah FORGE site have advantages of a fine spatial resolution of 1 m with a wide frequency range, but instrument

improvements are needed to increase the signal-to-noise ratio (SNR), make gauge length adjustable, correct fiber directivities, and develop multi-component DAS systems. 3C geophones can record vector wave fields and provide a complementary downhole tool to compensate disadvantages of current single-component fiber systems. The high-quality seismic waveforms recorded during Phase 2C of the Utah FORGE project can be used to refine relative event locations with waveform correlation methods, extract source time functions using an empirical Green's function method, and accurately measure rising times for reliable estimates of stress drops.

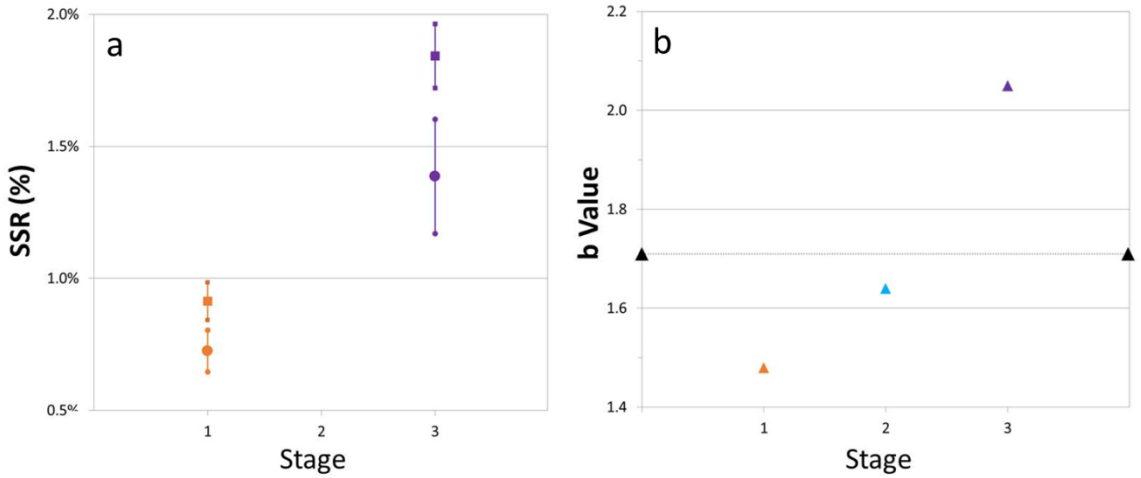


**Figure 15: Comparison of variations during stages of fracture stimulations for SSR values (a) and b-values (b). Both results show the apparent increase trends from Stage 1 to Stage 3. Average SSR values in (a) with one standard deviation are for the values in sedimentary (squares) and granite (solid circles) rocks. The b-value derived from all 424 events is shown by black triangles with the dotted line.**

We have used an existing micro-earthquake event catalog to characterize induced microseismicity at the Utah FORGE EGS site and found large micro-earthquakes with M > -0.999 occurred in Stage 2 of fracture stimulation concentrated in a small region close to the treatment well (58-32). We have derived b-values of 1.71 for all 424 induced micro-earthquakes occurred during the entire fracture stimulation tests. The b-values of induced micro-earthquakes in Stages 1, 2, and 3 of fracture stimulations are 1.48, 1.64, and 2.06, respectively, indicating a time-lapse increase of b-values from Stage 1 to Stage 3.

We have analyzed shear-wave splitting using 3C waveforms recorded with a 3C borehole geophone array. We have used 3C eigenvector rotation and waveform cross-corrections to separate faster and slower S-waves, determine their directions, and measure SSR (S-wave Splitting Rate) values in both granitic and sedimentary rocks. For six events in Stage 1, faster $S_1$-waves are along a radial direction at E12.7° ± 4.5°S, which is consistent with major-semi axis orientation of induced micro-earthquake distribution. SSR values of six microseismic events in Stage 1 range from 0.52% to 1.06%, with slightly higher values in sediments. Trends of the SSR curves are similar to that of sonic dipole logs. The average SSR values of 3 micro-earthquakes in Stage 3 range from 1.1% to 1.8%, which are higher than those measured in Stage 1. We hypothesize that this time-lapse increase of SSR values from Stage 1 to Stage 3 may be related to the highly fractured zones in granite rocks during Stage 2 fracture stimulation. Highly variable SSR values of 3 events in Stage 3 suggest high heterogeneities of the fracture zones created during Stage 2 stimulation. Time-lapse increase of SSR values from Stage 1 to Stage 3 coincides with the increase of b-values from Stage 1 to Stage 3. These time-lapse increases or variations of SSR values and b-values may reveal effectiveness and efficiency of fracture stimulations in EGS reservoirs.

## ACKNOWLEDGMENTS

The work at LANL was supported by the Geothermal Technologies Office of the U.S. Department of Energy (DOE) through the Los Alamos National Laboratory (LANL), which is operated by Triad National Security, LLC, for the National Nuclear Security Administration (NNSA) of U.S. DOE under Contract No. 89233218CNA000001.

## REFERENCES

Geffers, G-M., Main, I.G., Naylor, M.: "Biases in estimating b-values from small earthquake catalogues: how high are high b-values?" Geophysical Journal International, Volume **229**, (2022), Pages 1840–1855, https://doi.org/10.1093/gji/ggac028

Li, X.-Y., Mueller, M. C. and Crampin, S.: "Case studies of shear-wave splitting in reflection profiles in South Texas," Canadian Journal of Exploration Geophysics, **29**, (1993), 189–215.

Li, Y., & Hewett, B.: Reflection salt proximity, First Break, **34**(10), (2016), 33–39, https://doi.org/10.3997/1365-2397.2016011

Li, Y., Karrebach, M., and Ajo-Franklin J.: A Literature Review: Distributed Acoustic Sensing (DAS) Geophysical Applications over the Last 20 Years. In: Distributed Acoustic Sensing in Geophysics: Methods and Applications, Geophysical Monograph **268**, (2021), 231-293,

Lou, M., and Rial, J. A.: Characterization of geothermal reservoir crack patterns using shear-wave splitting, Geophysics, **62**, (1997), 487–494. https://doi.org/10.1190/1.1444159

Moore, J., McLennan, J., Pankow, K., Simmons, S., Podgorney, R., Wannamaker, P., Jones, C., Rickard, W., & Xing, P.: The Utah Frontier Observatory for Research in Geothermal Energy (FORGE): A Laboratory for Characterizing, Creating and Sustaining

Enhanced Geothermal Systems. In: Proceedings (SGP-TR-216), 45th Workshop on Geothermal Reservoir Engineering, Stanford University, CA, USA (2020).

Munson C.G., Thurber, C.H., & Li, Y.: Observations of shear wave splitting on the southeast flank of Mauna Loa Volcano, Hawaii, Geophys. Res. Lett., **20**, (1993), 1139-1142. https://doi.org/10.1029/93GL01213

Munson, C.G., Thurber, C.H., Li, Y., & Okubo, P.G.: Crustal shear-wave anisotropy in Southern Hawaii, J. Geophys. Res., **100**, (1995), 20367-20377. https://doi.org/10.1029/95JB01288

Pankow, K., Mesimeri, M., McLennan, J., Wannamaker, P., & Moore J.: Seismic Monitoring at the Utah Frontier Observatory for Research in Geothermal Proceedings (SGP-TR-216), 45th Workshop on Geothermal Reservoir Engineering, Stanford University, CA, USA (2020).